Nanoscale Advances

ROYAL SOCIETY OF CHEMISTRY

PAPER

View Article Online
View Journal | View Issue

Cite this: *Nanoscale Adv.*, 2023, **5**, 2470

Tuning of MgO's base characteristics by blending it with amphoteric ZnO facilitating the selective glucose isomerization to fructose for bioenergy development†

Sangeeta Mahala,[ab] Senthil M. Arumugam,[a] Sandeep Kumar,[a] Bhawana Devi[ab] and Sasikumar Elumalai *[a]

Fructose serves as an important intermediate in the preparation of liquid fuel compounds. Herein, we report its selective production *via* a chemical catalysis method over ZnO/MgO nanocomposite. The blending of an amphoteric ZnO with MgO reduced the latter's unfavorable moderate/strong basic sites that can influence the side reactions in the sugar interconversion, reducing fructose productivity. Of all the ZnO/MgO combinations, a 1 : 1 ratio of ZnO and MgO showed a 20% reduction in moderate/strong basic sites in MgO with ~2–2.5 times increase in weak basic sites (overall), which is favorable for the reaction. The analytical characterizations affirmed that MgO settles on the surface of ZnO by blocking the pores. The amphoteric ZnO undertakes the neutralization of the strong basic sites and improves the weak basic sites (cumulative) by the Zn–MgO alloy formation. Therefore, the composite afforded as high as 36% fructose yield and 90% selectivity at 90 °C; especially, the improved selectivity can be accounted for by the effect of both basic and acidic sites. The favorable action of acidic sites in controlling the unwanted side reactions was maximum when an aqueous medium contained 1/5th methanol. However, ZnO's presence regulated the glucose's degradation rate by up to 40% compared to the kinetics of pristine MgO. From the isotopic labelling experiments, the proton transfer pathway (or LdB–AvE mechanism by the formation of 1,2-enediolate) is dominant in the glucose-to-fructose transformation. The composite exhibited a long-lasting ability based on the good recycling efficiency of up to 5 cycles. The insights into the fine-tuning of the physicochemical characteristics of widely available metal oxides would help develop a robust catalyst for sustainable fructose production for biofuel production (*via* a cascade approach).

Received 13th February 2023
Accepted 23rd March 2023

DOI: 10.1039/d3na00097d

rsc.li/nanoscale-advances

Introduction

5-Hydroxymethylfurfural (HMF), a furanic platform chemical, is an established versatile and potential chemical in the manufacture of liquid biofuels and biopolymer compounds (including 2-methylfuran, 2,5-dimethylfuran, 2,5-diformylfuran, levulinic acid, 2,5-furandicarboxylic acid, and 2,5-bis(hydroxymethyl)furan).[1,2] For its synthesis, many researchers choose glucose as a feedstock because of its large availability in the form of cellulose, which is present up to 50% in the lignocellulosic materials that are abundant and underutilized. However, the direct glucose conversion to HMF involves a series of transformations, such as glucose isomerization to fructose, followed by dehydration to HMF. Of the transfers, glucose into fructose is a slower step due to the equilibrium characteristics.[3] To date, a biotechnological approach is widely followed to produce fructose that is used to produce high-fructose corn syrup rich in glucose,[4] especially for food additive applications.[5] However, this approach faces several challenges, including downstreaming of the product, prolonged reaction times, and frequent enzyme activity loss. Meanwhile, several chemical systems, such as homogenous and heterogenous, have been developed to produce fructose as simply as possible, *i.e.*, within 5–180 min over mineral reagents, for biofuel applications.[6,7] It can be produced over acid or basic catalysts, but they follow dissimilar pathways.[6] An acid catalyst can induce the 1,2-hydride shift in glucose to form fructose by initially having an interaction at O-1 of glucose by the acidic sites, leading to the development of polarization at C=O to form fructose.[8] On the contrary, the base catalyst firstly synthesizes an enediol intermediate due to the abstraction of a proton at O-2 followed by fructose formation by following the Lobry de Bruyn–Alberda van

[a]*Chemical Engineering Division, DBT-Center of Innovative and Applied Bioprocessing, Mohali, Punjab 140306, India. E-mail: sasikumar@ciab.res.in; Tel: +91-172-5221-444*
[b]*Department of Chemical Sciences, Indian Institute of Science Education and Research (IISER), Mohali, Punjab 140306, India*

† Electronic supplementary information (ESI) available. See DOI: https://doi.org/10.1039/d3na00097d

Ekenstein mechanistic theory (LdB–AvE).[9] However, the chemical setups are able to achieve only 30% fructose and 60% selectivity (on average), mainly caused by the routine side reactions by utilizing the reactant and/or product.[6] For improving fructose productivity, tireless continuous efforts are made to design an effective catalytic system, especially a solid catalyst, because of its advantages that it can be reused multiple times and regenerated quickly.[6,10,11] Moreover, its catalytic properties can be fine-tuned to promote a specific reaction of interest.[12] Within the naturally occurring solid catalyst, metal oxides (*e.g.*, TiO_2, ZrO_2, MgO, CaO, Nb_2O_5, CeO_2, and SiO_2) are popular because of their catalytic proficiency attributed to the inherently favorable characteristics, including acidity/basicity (Lewis and/or Brønsted strengths, which are tuneable) and redox features.[13–18] In fructose synthesis, a Lewis acid or base condition is documented to be operative;[6,19,20] therefore, many have employed the composite formulation or doping techniques to modify the intrinsic characteristics of the natural metal oxide catalysts to nominate a potential candidate for the reaction and a scalable catalyst for process development. For instance, recently, Arumugam *et al.* have regulated the strong base characteristics of CaO by incorporating MgO, which has a relatively large number of weak base sites. Thereby offering a favorable condition for glucose isomerization and yielding as high as 33% fructose and 80% selectivity in a shorter time (15 min).[16] In another study, Otomo *et al.* showed the effectiveness of SiO_2 after ammonia treatment by achieving a fructose yield of up to 35 and 91% selectivity. However, it exhibited poor recyclability, *i.e.*, only 7.4% fructose yield after 4 recycles due to the accelerated removal of nitrogen content (~56%).[17] Also, the catalyst preparation was laborious.

Considering the catalyst's durability, low cost, facile synthesis, and suitability for glucose isomerization, in the present study, a composite of basic MgO and amphoteric ZnO was developed by following a conventional sol–gel protocol. The characteristic MgO represents a nano-size particle that measures ~50 nm and exhibits weak base sites predominantly (>100 μm g^{-1} CO_2), which is favorable for interconversion reaction.[6,14,16,21] Marianou *et al.* demonstrated the potential of MgO (containing 1% CaO as an impurity) in the glucose into fructose conversion, attributed to its weak basicity, which is dependent on crystal size, surface area, and chemical composition.[14] However, the impurity offering additional strong basic sites affected the selectivity of fructose *via* unwanted sugar degradations, therefore, it reported an average fructose yield (33%) with 76% selectivity through a 44.2% glucose conversion under modest conditions. In a typical reaction, Brønsted (or strong) base conditions can influence several unwanted degradation reactions, resulting in numerous sugar-derived acids (including lactic acid), which can further influence the fructose to undergo dehydration to form HMF, thereby reducing the product concentration and selectivity.[9] In addition, MgO itself contains considerable moderate/strong base sites (≤50 μm g^{-1} CO_2). For specifically reducing the impact of the unfavorable basic sites in MgO, a substantial nano-size ZnO was added to represent a ZnO/MgO nanocomposite. The characteristic ZnO is an amphoteric material;[22] therefore, it can regulate the strength of strong basic sites *via* neutralization by the inherent acidic sites. It can also contribute favorably to increasing the number of weak basic sites. But it measures as a large-size nanoparticle (~100 nm) with a hexagonal structure;[23] therefore, obviously, it may accommodate the MgO on its surface while blending.[24] In that case, presumably, the architecture of the nanocomposite catalyst is such that MgO blocks the ZnO's pores and offers maximum weak basic sites that can administer the reaction and improve fructose productivity.[21] In this way, ZnO can play a vital role in modulating the base characteristics of MgO and enabling a selective glucose transformation.

Experimental

Chemicals and reagents

All chemicals and reagents, including D-glucose, D-fructose, D-mannose, HMF, ethanol, methanol, magnesium sulfate monohydrate ($MgSO_4 \cdot H_2O$), deuterium oxide (D_2O, 99.9 atom% D), zinc acetate dihydrate [$Zn(CH_3COO)_2 \cdot 2H_2O$] and sodium hydroxide (NaOH, 50% wt) were purchased from Sigma-Aldrich (India). Deuterated glucose at C2 (D-[2-^{2}H]glucose) was purchased from Omicron Biochemicals Inc. (Indiana, USA). All purchased chemicals were of analytical grade and used as received. The Millipore water purifier system was used to produce the deionized water (DI) and used in the sample preparations and dilutions.

ZnO/MgO nanocomposite formulation

A conventional sol–gel method was employed to synthesize ZnO/MgO nanocomposite, as reported elsewhere.[22] Briefly, 20 mL 0.5 M of metal salt solutions using $MgSO_4 \cdot H_2O$ (1.2037 g) and $Zn(CH_3COO)_2 \cdot 2H_2O$ (2.1951 g) were prepared separately using the DI water in a 50 mL beaker. To these individual metal salt solutions, 5 mL of 0.3 M NaOH was added gradually under a stirring condition. After 24 h of continuous stirring at room temperature, both solutions were mixed together, then 10 mL of 2 M NaOH solution was added and continued the stirring for another 24 h. The formed precipitate was separated *via* high-speed centrifugation (8000 rpm). It was sequentially washed using DI water and ethanol–water mixture and dried at 70 °C overnight. The dried solid was ground using mortar-pestle followed by calcinated using a programmable muffle furnace (Thermo Fisher) at 800 °C at 2 °C min^{-1} rate for 3 h. The resultant white solid residue was labelled as ZM11. A similar protocol was followed to prepare a different ZnO/MgO composite, for which, 0.5 M $Zn(CH_3COO)_2 \cdot 2H_2O$ (2.1951 g) and 0.25 M $MgSO_4 \cdot H_2O$ (0.6018 g) were used to formulate ZM21 catalyst, and 0.25 M $Zn(CH_3COO)_2 \cdot 2H_2O$ (1.0975) and 0.5 M $MgSO_4 \cdot H_2O$ (1.2037 g) were used for ZM12. The reference ZnO and MgO catalysts were prepared by following a similar protocol but using 0.5 M $Zn(CH_3COO)_2 \cdot 2H_2O$ or 0.5 M $MgSO_4 \cdot H_2O$ precursors, respectively.

Analytical characterization techniques

The crystallographic structure and phase purity determination of the as-synthesized catalysts were performed using the X-ray

diffractometer (XRD; Rigaku Smart LAB SE). The machine was equipped with a Cu Kα radiation source of $\lambda = 1.540593$ Å. The samples were scanned from the 10° to 80° range. The crystal size was calculated using the Debye–Scherrer equation ($D = K\lambda/\beta \cos\theta$), where K is the Scherrer constant (considered as 0.9), λ is the wavelength, β is the full width at half maximum height (FWHM) of the sharp peaks and θ is the measured angle. The functional group determination was made using the Fourier transform-infrared spectrometer (FTIR; Agilent Technologies Cary 600 series). The surface morphology was analyzed using the field-emission scanning electron microscopy instrument (FE-SEM; HITACHI, SU8010, and Thermo Fisher Apreo 2). The elemental fraction determination and elemental mapping were made using the embedded energy-dispersive X-ray spectroscope unit (EDX). The size and shape determinations were made using the high-resolution transmission electron microscope instrument (HRTEM; JEOL-JEM-2100 Plus). For the analysis, the sample was prepared by uniformly dispersing in ethanol and placing some of it on a carbon-coated grid. The elemental composition analysis was made using the inductively coupled plasma-mass spectrometer (ICP-MS; Agilent Varian 715-ES ICP Optical emission spectrometer). Prior to the analysis, the catalyst was digested in 10 mL ICP MS-grade HNO_3 using a microwave digester (CEM Mars 6). The electron structure and oxidation states of metal ions were determined using the X-ray photoelectron spectrophotometer (XPS; PHI 5000 VersaProbe III). The surface area, pore volume, and pore size determinations were performed using the BET analyzer (Quantachrome Autosorb iQ) by recording the nitrogen adsorption–desorption isotherms. The total pore volume was calculated by measuring the amount of N_2 adsorbed at a relative pressure (P/P_0) of 0.99. The average pore diameter and volume were calculated by following the Barrett–Joyner–Halenda (BJH) method. For the analysis, the sample was degassed at 120 °C for 8 h. The acidic and basic sites of the catalysts were determined by temperature-programmed desorption of ammonia (NH_3-TPD) and carbon dioxide (CO_2-TPD), respectively, using the BELCAT II instrument, which was equipped with a TCD detector. For this, 55 mg catalyst was packed in a quartz tube and heated from room temperature to 500 °C under a He gas stream of 50 mL min^{-1} for 60 min. After the degassing procedure, the hot material was cooled down to 50 °C and the CO_2 and NH_3 adsorption was performed under the continuous He flow (50 mL min^{-1}) condition. The desorption studies were carried out between 50 and 750 °C at the ramp rate of 10 °C min^{-1}.

Glucose isomerization to fructose over MgO/ZnO composite

In typical batch glucose isomerization, 0.4% wt glucose (aqueous/alcohol) was loaded in a 35 mL glass reactor. A varying solid catalyst supply was made from 1 : 12 to 1 : 4 wt on glucose. The sealed reactor was heated (up to 100 °C) in an oil bath for up to 165 min under a stirring condition. After a specified time, the reactor was removed and quenched immediately in an ice bath to arrest the reaction. The post-reaction mixture was collected and centrifuged at 8000 rpm to separate the liquid and solid portions. From the liquid portion, an aliquot was collected, diluted using DI water, and analyzed on a high-performance liquid chromatograph instrument (Thermo Scientific, Dionex Ultimate 3000 series) equipped with an RI detector (maintained at 50 °C). An Agilent Hi-Plex Ca column (maintained at 80 °C) was used for the chemical analysis. HPLC-grade water was used as an eluent flowing at 0.6 mL min^{-1}. The yield, selectivity, and conversion calculations were made using the expressions (eqn (S1)–(S3)) present in the ESI† and by using calibration charts prepared using commercial chemicals. Meanwhile, the collected solid was thoroughly washed using an ethanol–water mixture followed by oven-dried at 70 °C overnight for reusing. The recyclability study was conducted by following a similar protocol but with a recovered catalyst. All the experiments were duplicated. The data were analyzed using the SPSS software for ANOVA analysis. For the product formation confirmation, the collected liquid portion was freeze-dried and dissolved in 1 mL D_2O. The NMR analysis was performed using a 500 MHz Bruker Avance Neo NMR spectrophotometer equipped with a DCH cryoprobe. The recorded ^1H and ^{13}C NMR spectra were analyzed using Mnova software.

Isotopic labelling experiment and NMR characterization

The reaction mechanism was confirmed *via* an isotopic labelling experiment. For this, a similar isomerization protocol was followed but with a different substrate and reaction medium. In Exp-I, labelled glucose (deuterated at C2) was used as a substrate in DI water. Whereas, in Exp-II, unlabelled glucose was used as a substrate in the D_2O medium. These separate isomerization reactions were conducted under similar conditions. Upon completion of the reaction, the respective post-reaction mixtures were collected and the solid catalyst was separated *via* high-speed centrifugation (~8000 rpm). The liquid portion was freeze-dried and dissolved in 1 mL D_2O for NMR analysis. A 500 MHz Bruker Avance Neo NMR spectrophotometer equipped with a DCH cryoprobe was used.

Results and discussion

Analytical characterization of the as-synthesized ZnO/MgO catalyst(s)

Fig. 1a shows the comparative XRD result of pristine (ZnO and MgO) and nanocomposite metal oxides (such as ZM11, ZM21, and ZM12). Apparently, all catalyst materials exhibited characteristic intense and narrow diffraction peaks, suggesting their highly crystalline nature.[16] The pristine ZnO exhibited peaks at 31.3°, 34.0°, 35.8°, 47.1° and 56.2° corresponding to (100), (002), (101), (102), (110) miller indices planes, affirming ZnO's wurtzite phase with zincite structure,[22] based on the JCPDS card = 36-1451, $P6_3mc$. Similarly, MgO had typical diffraction peaks at 35.7°, 42.3°, and 61.8° corresponding to the (111), (200), and (220) planes, confirming its periclase phase,[16] according to JCPDS card = 04-8209, $Fm\bar{3}m$. Whereas, the composites presented obvious merged results, specifically ZM11 and ZM12. ZM21 did not show the corresponding peaks for MgO, this strange behavior insisted on analyzing the XRD pattern. ZnO's peaks in all composites, mainly (100), (002), and (101), can be

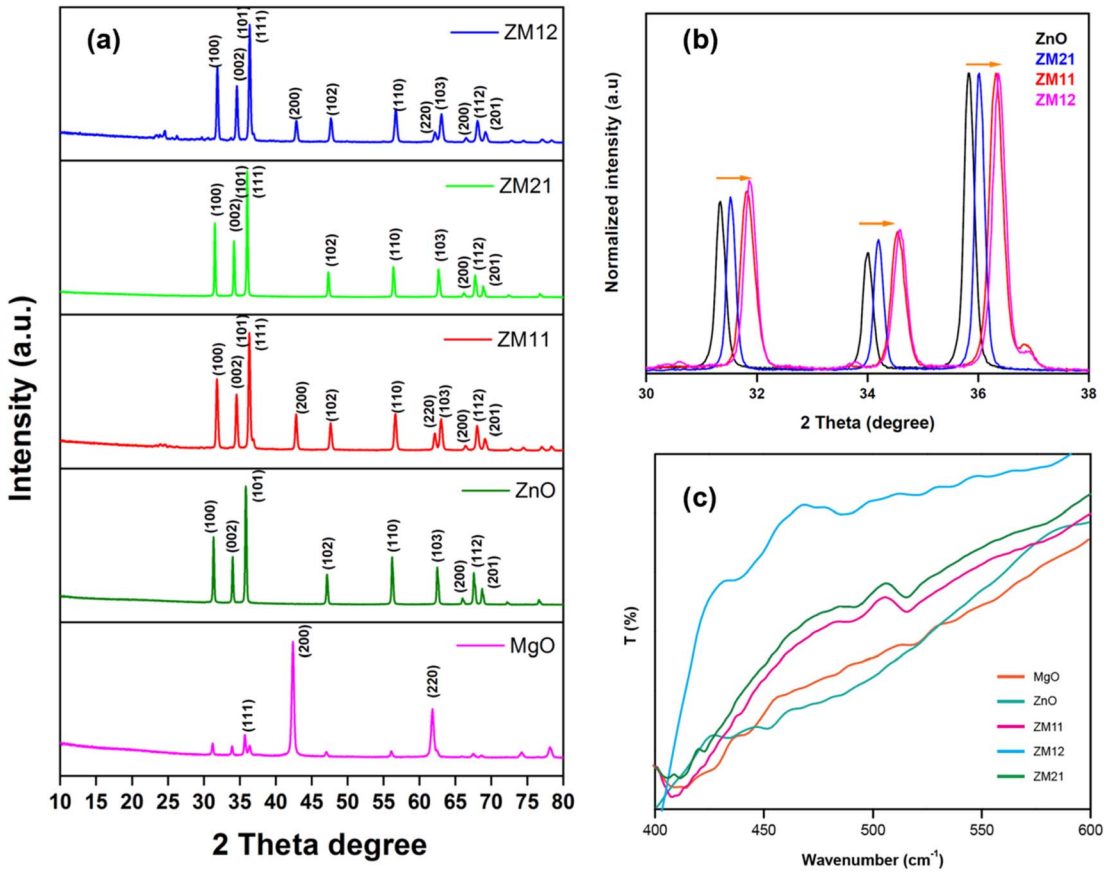

Fig. 1 Comparative characterization results of the as-synthesized catalyst(s): (a) XRD analysis report, (b) normalized XRD analysis result and (c) FTIR analysis short-range report.

seen shifted towards a higher 2θ angle, suggesting the displacement of Mg into the ZnO's lattice.[16,25,26] This can be a valid reason for the missing MgO ($1/4^{th}$ level) peak in ZM21, as maximum Mg has already been dislocated to the inner lattice of ZnO. This lattice diffusion in ZnO can be verified from the *d*-spacing values and shifts in the peaks (Fig. 1b). Other composites exhibited all respective peaks of both metal oxides but with varying MgO's peak intensity because of a different supplementation. Moreover, the remarkable peak shift and broadening of peaks corresponding to the incremented Mg in the composites suggest higher Mg lattice diffusion into ZnO. The composites' respective peak shift, peak boarding, and *d*-spacing values of ZnO's (100), (002), and (101) planes can be found in Tables S1–S3.† The results clearly show the nearly identical characteristics of ZM11 and ZM12. The *d*-spacing value for the (002) plane in pristine ZnO was estimated as 2.63 Å; however, the value was shifted towards the down range for the composites as 2.61 Å (for ZM21) and 2.59 Å (for ZM11 and ZM12 having a higher Mg concentration). This indicates the winding of ZnO's lattice due to the binding of a lower ionic radii Mg^{2+} (66 pm) compared to Zn^{2+} (74 pm); from this, the diffusion of Mg into ZnO is quite possible *via* substitution, thereby enabling the alterations in the lattice plane.[28] Due to this, the crystalline size of the nanocomposites got affected, such as the pristine ZnO was measured to be 49.56 nm, while ZM21, ZM11, and ZM12 were measured as 46.07, 32.71, and 33.35 nm, respectively. These results somewhat affirm the successful dislocation of Mg into ZnO's lattice plane (002). Moreover, except for the ZM21, other composites can have surface MgO because of its load in excess of saturation, *i.e.*, >30% molar concentration. A similar variation was observed in the results of (100) and (101) planes of ZnO, as data are present in Tables S1–S3.† The effect of diffusion of Mg into the ZnO's planes can be determined from the crystal structure parameters, such as *C*-axis length, lattice strain (ε), lattice stress (σ), and dislocation density (δ), using eqn (S4)–(S6)†. Table 1 displays the parameter values of the ZnO's crucial (002) plane for all the catalysts, including pristine metal oxides. From the results, the introduction of Mg into ZnO's crystal lattice makes a notable change in the composite's crystal structure, for instance, the *C*-axis

Table 1 Crystal structure parameters of ZnO's (002) plane in all synthesized catalysts

Parameters	ZnO	ZM21	ZM11	ZM12
C-axis length (Å)	5.260	5.220	5.184	5.180
Lattice strain (ε, 10^{-4})	25.00	26.74	37.32	36.54
Lattice stress (σ, 10^{11}/Nm^2)	−0.046	−0.012	0.019	0.022
Dislocation density (δ, 10^{-4}/nm^{-2})	4.09	4.27	10.35	10.50

length of the ZnO decreases with an increasing concentration of the lattice Mg content. Likewise, the lattice stress and strain of the ZnO's can be seen increased by Mg's incorporation, especially with ZM11 and ZM12, the lattice stress increased up to 46–49% (positive strain).[24,27] A remarkable change in the dislocation density also confirmed the incorporation of Mg in ZnO, based on a nearly 2-fold increased value, suggesting that Mg can create more lattice disorders. But the parameter values of ZM11 and ZM12 appeared nearly equal, indicating less impact of Mg when loaded above the saturation limit (*i.e.*, in this case, >50%).

The FTIR characterization results (Fig. 1c and S1†) disclose the absence of surface hydroxyl groups in the catalysts based on the nil appearance of significant peaks under the higher wavenumber range (3000–3500 cm^{-1}).[22,25] In the results of ZnO, the notable peaks at 432 cm^{-1} and 452 cm^{-1} are attributed to Zn=O bond stretching frequency. The pristine MgO exhibited dominant peaks at 410 cm^{-1}, 443 cm^{-1} and 520 cm^{-1} corresponding to the metal–oxygen stretching frequency.[16,18] A set of weaker and broaden peaks observed at 1114 cm^{-1} and 1457 cm^{-1} belong to the bending and stretching vibrations of –OH and C=O, respectively, which are the surface absorbed moisture and CO_2 contents.[26] The composites had several matching peaks but with varying intensities depending on the concentration. They also experienced obvious peak shifting at higher wavenumbers, caused by an intrinsically strong interaction between the metal oxides. But the interaction between metal and oxygen may have a weaker bond strength. Specifically, ZM11 exhibited vibrant peaks at 408 cm^{-1}, 490 cm^{-1}, and 515 cm^{-1}, which are the regulated vibrations of both metal oxides.[27] The ZM12 presented both metal oxide peaks at 408 cm^{-1}, 423 cm^{-1}, 493 cm^{-1} and 515 cm^{-1} that established an obvious MgO dominance. Contrarily, ZM21 exhibited lower MgO characteristics, based on a weak peak observed at 526 cm^{-1} corresponding to the MgO's stretching frequency and the sharp peaks at 435 cm^{-1} and 489 cm^{-1} relative to ZnO.

The binding energy and chemical environment of the metal ions in the catalysts were determined *via* XPS analysis in the 0–1350 eV measurement range. All peaks were calibrated using C 1s as an internal reference at 292.8, 285.93, and 285.08 eV for pristine (MgO and ZnO) and composites. Fig. 2a–i shows the

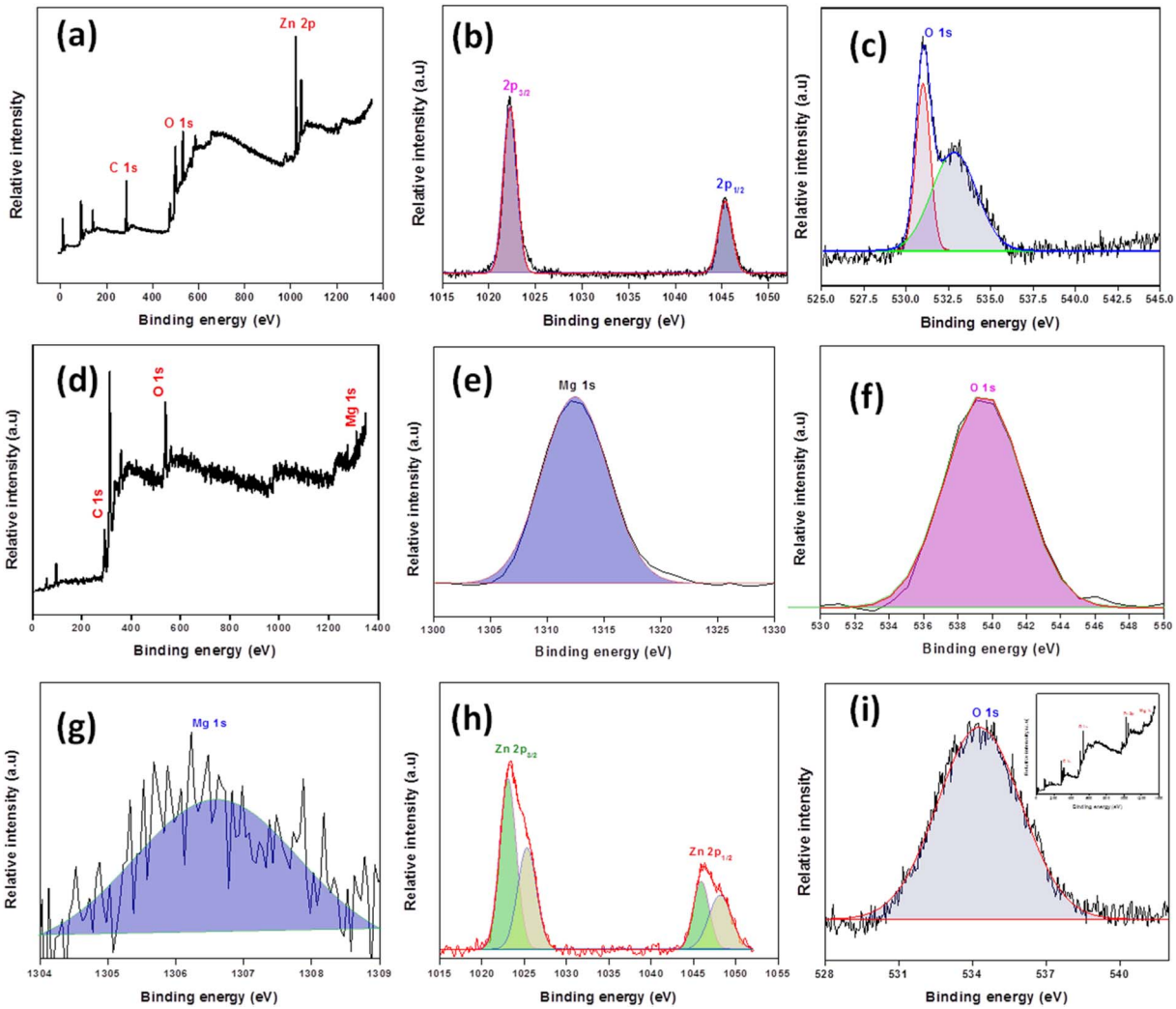

Fig. 2 XPS characterization results of ZnO (a–c), MgO (d–f), and ZM11 (g–i); inset: XPS survey report).

comparative survey spectrum of the catalysts; in the spectra, a slight shift can be noted, likely caused by the metal oxides interaction, consistent with XRD and FTIR analyses. The results of ZM11 show (Fig. 2g–i) that the Zn 2p spectrum has four peaks at 1023.7 and 1025.39 eV corresponding to Zn $2p_{3/2}$, and 1046.18 and 1048.39 eV corresponding to the Zn $2p_{1/2}$ states.[28,29] Specifically, the lower binding energy peaks (1023.7 and 1046.18 eV) designate the Zn^{2+} state of ZnO. The other two peaks (1025.39 and 1048.39 eV) are assigned to the Zn^{2+} state present in the Zn–MgO complex (alloy) formed *via* lattice incorporation of Mg into ZnO.[27] But, upon deconvolution of spectra of Zn 2p of ZnO, it produced two sharp peaks at 1023.7 and 1046.18 eV corresponding to the $2p_{3/2}$ and $2p_{1/2}$ states of Zn^{2+} ions (Fig. 2a–c), respectively. This confirms that Mg has influenced the Zn^{2+}'s binding energy during migration into the ZnO's lattice plane, leading to the generation of a new chemical environment around Zn (as Zn–MgO). The spectra of O 1s of ZnO exhibited two peaks at 530.9 and 532.9 eV (Fig. 2c), which can be interpreted as enriched oxygen (O^{2-}) present in the ZnO's crystal lattice plane. However, the higher binding energy peaks are interpreted as the oxygen vacancy or loosely bounded oxygen on ZnO's surface, which could be the O_2 absorbed during analysis. Contrarily, the ZM11 exhibited a single peak at 534.6 eV, attributed to the oxygen in one chemical environment, confirming its predominant metal oxide form. It could be possible that the interacting MgO has reduced the loosely bounded oxygen molecules or oxygen vacancies in ZnO, as a result, ZM11 exhibited a single oxygen environment. Mg in pristine MgO and ZM11 exhibited common peaks at 1312.5 and 1306 eV, corresponding to the Mg 1s (Fig. 2e and g). Suggesting that MgO retains its own chemical nature even when present in ZnO's crystal lattice. From the results of pristine MgO, the oxygen has one oxygen environment and it does not contain hydroxides, affirming that the oxide formation is only with Mg. However, the ZM11 composite exhibited a remarkable peak shift in all the elemental peaks compared to the pristine ones (as shown in Table S4†), likely caused by the formation of Zn–MgO alloy and the synergetic interaction between the metal oxides.[25] While analyzing the results of the other two composites (ZM12 and ZM21), they showed no peak splitting for the Zn^{2+} state. Moreover, the element peak pattern resembled the results of the pristine metal oxides. Suggesting, no formation of a new metal alloy (Fig. S2†). However, the observed small peak shift is caused by the effect of the interaction between the metal oxides. The results agree with the findings of the XRD analysis that the lattice incorporation of Mg is common in all composites but ZM11 is exceptional in an alloy formation. This is likely attributed to the strong interaction enabled between the incorporated Mg and ZnO that is facilitated by an equal ratio composition. This can be evident from the results of ZM21, which show that it has only a weak lattice interaction between Mg and ZnO, despite the complete dislocation of Mg into the crystal lattice. Only 1s peak was observed in the XPS spectra of the catalysts and that corresponded to Mg^{2+} ions, ruling out the metallic form of Mg. Moreover, the poor interaction between the incorporated Mg and ZnO led to a minute small peak shift in the Zn^{2+} peak (0.56 eV). In addition, the results of ZM12 support the assumption based on a close resemblance of the survey spectrum. However, it exhibited a significant peak shift with Zn^{2+} (0.70 eV), caused by the more migration of Mg into the ZnO's lattice, attaining a higher interaction strength. Moreover, in ZM12, the MgO nanoparticles appeared to be more dominant than Mg, due to this, a reduced alloy formation could be achieved, leading to the yielding of a single peak for Zn^{2+}. Thus, the results imply that more Mg load can increase its migration into ZnO's lattice, but their interaction is more upon the formation of a new alloy, whose extent is favorable under a proportionate metal oxide supply condition.

The morphological analysis by FE-SEM indicated that the ZnO contains both pseudo-hexagonal and spherical morphologies[28,29] and is bigger in size compared to MgO (Fig. 3i). MgO exhibited a distinctive morphology, *i.e.*, tiny and spherical in shape[14,16] (Fig. 3ii). Obviously, the ZM11 showed mixed characteristics of both MgO and ZnO (Fig. 3iii), with a uniform distribution of MgO on the ZnO's surface, representing a spherical and basil-type structure.[30] The vivid images captured during SEM-EDX analysis substantiate the wide distribution of MgO in ZM11 (Fig. 3iv). The analysis also determined the elemental composition as 25% of Zn, 21% of Mg, and 54% of O (atom) (Fig. S4†), consistent with the ICP-MS analysis data (Table S5†). The results of ZM21 and ZM12 verify the influence of MgO on the catalyst's morphology (Fig. 3v and vi). ZM21 having a lower Mg present in the ZnO's lattice exhibited the least impact on the morphology, therefore, the catalyst represented the maximum characteristics of ZnO. But in ZM12, MgO's impact can be seen as significant, *i.e.*, molding the catalyst into a rigid particle and deforming the hexagonal structure of ZnO by in-between diffusion (Fig. 3vi).[24] The mapping results validate the consistent elemental concentration of the catalysts (Fig. S3 and S4†). Comparatively, ZM12 exhibited unique characteristics attributed to the widespread deposition of an excess MgO on ZnO, affecting the shape of the backbone ZnO. It could be possible that MgO activates the aggregation of ZnO. The HR-TEM analysis report authorizes the catalysts' crystallinity and particle sizes (Fig. 3a–i); most MgO nanoparticles exhibit a spherical shape measuring in the 20 nm to 100 nm range,[16] with a respective electron orientation (Fig. 3a and b), based on the particle size distribution curve (Fig. 3c). The pristine ZnO is represented as the largest size particle, measuring a 100–220 nm range, of a hexagonal shape[31] (Fig. 3d–f). ZM11 exhibiting a similar size range of 20–100 nm as ZnO reinforced the speculation that MgO undergoes a lattice diffusion into ZnO, whereby having a strong interaction (Fig. 3g–i), consistent with the XRD analysis (Fig. 1a). Thus, the results manifest the structural architecture of the nanocomposite catalyst (ZM11) that has a significant amount of MgO attached to the surface of ZnO.

The conventional Brunauer–Emmett–Teller (BET) method was employed to gain the surface area, pore volume, and pore size distribution details of the catalysts. The recorded N_2 adsorption–desorption isotherms (Fig. S4†) were found to be obeying the type-IV hysteresis loop of the IUPAC classification.[32] The influence of the catalyst's inherent chemical composition on the surface characteristics can be witnessed from the BET

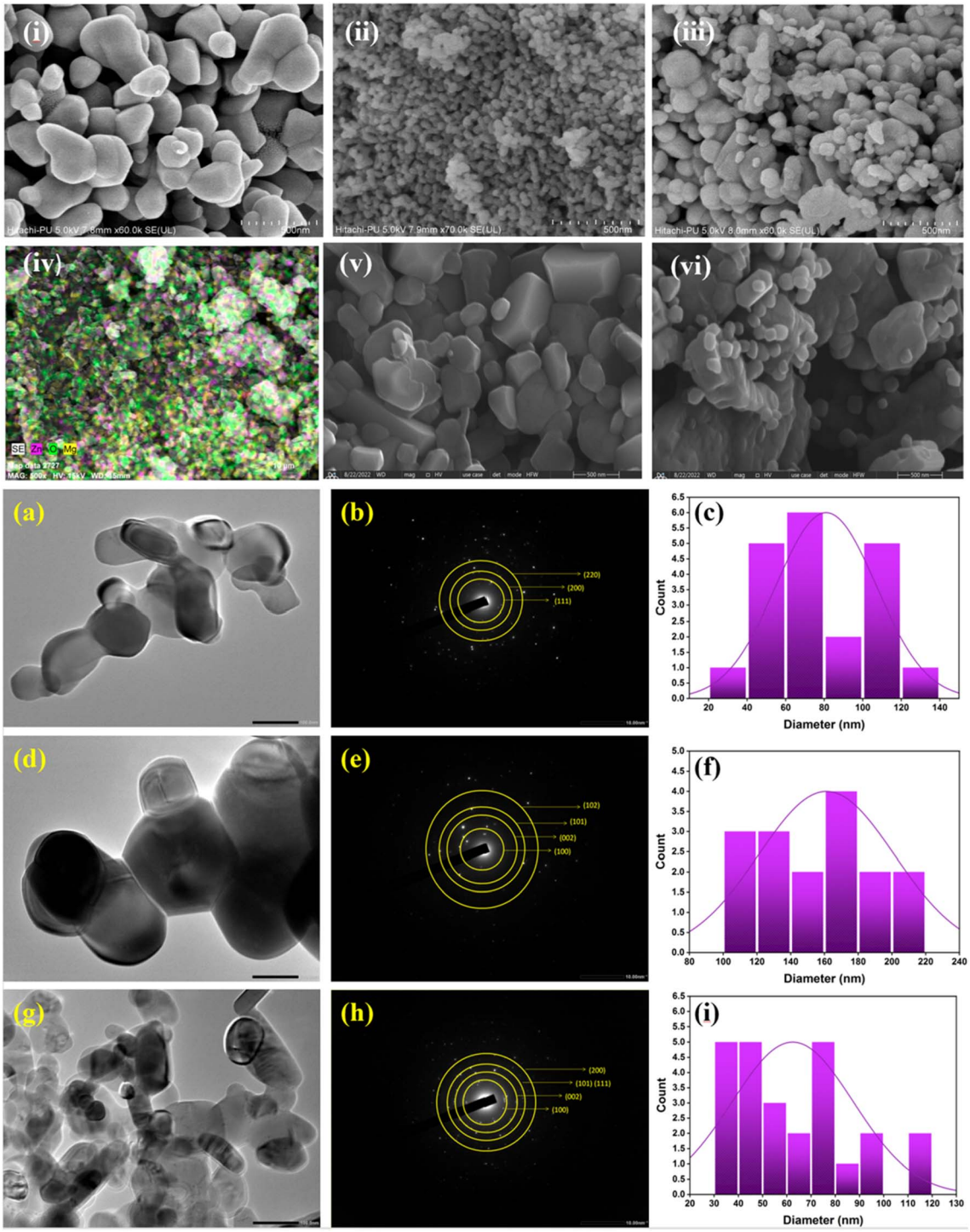

Fig. 3 FE-SEM analysis report of ZnO (i), MgO (ii), ZM11 (iii), mapping result of ZM11 (iv), ZM21 (v), and ZM12 (vi), and HR-TEM analysis report (with SAED image and particle size histogram) of MgO (a, b and c), ZnO (d, e, and f), and ZM11 (g, h and i).

and BJH adsorption isotherms. Pristine MgO and ZnO exhibited a pore size of 2.45 and 2.18 nm with a surface area of 10.6 $m^2 g^{-1}$ and 18.6 $m^2 g^{-1}$, respectively[14,16] (Table 2), indicating that ZnO offers a 75% higher surface area.[33] Whereas, the ZM11 measured even better surface properties, *i.e.*, 2.73 nm and 26.8 $m^2 g^{-1}$ of pores size and surface areas, respectively, which is likely attributed to the Mg's diffusion into the ZnO lattice and their conjugation.[25] Therefore, it had a higher pore volume of 0.379 cm^3. This improved surface area can also be interpreted as the blockage of ZnO's pores by the MgO. However, the other composites showed lower surface properties than ZM11, which is likely caused by the imbalance in the ratio of MgO/ZnO, therefore exhibiting the characteristics of the dominant metal oxide, *i.e.*, higher ZnO content in the composite had maximum

Table 2 Results of surface properties measurement (physisorption and chemisorption) of catalysts

Catalyst	Surface area[a] ($m^2\ g^{-1}$)	Pore diameter[b] (nm)	Pore volume[b] (cm^3)	Acidic sites[c] ($\mu mol\ g^{-1}$)	Basic sites[c] ($\mu mol\ g^{-1}$)	
				Weak	Weak	Moderate/strong
MgO	10.6	2.45	0.036	31	85	60
ZnO	18.6	2.18	0.043	29	9	3
ZM11	26.8	2.73	0.379	60	121	48
ZM21	9.6	1.53	0.032	31	12	4
ZM12	8.2	1.94	0.020	29	104	29

[a] BET method. [b] BJH method. [c] Chemisorption.

corresponding characteristics and *vice versa* (Table 2). Besides, ZM12 with a high MgO has possibly influenced the ZnO aggregation, affecting the surface area of the composite; however, it exhibited nearly the same characteristics as pristine MgO. Contrarily, its lower ratio can refine the internal architecture of the composite due to displacement, resulting in a decreased pore size as observed with ZM21, leading to delivering a microporous material with a decreased surface area. Thus, the results infer that a balanced ratio of metal oxides can deliver a material of specific qualities for the catalytic reaction. An improved surface area of ZM11 can expose a higher number of active sites for binding of the reactant molecules; therefore, an enhanced conversion can be attained.[14,34] The attained wider pore is an added advantage because the reactant molecules (glucose measures ~1 nm in size) can be trapped, which is beneficial to glucose interconversion.[35] Thus, the internal diffusion of Mg into ZnO has decreased the particle size and improved the surface area and pore volume. The analysis also determined the acidic and basic strengths of the catalysts using the temperature-programmed desorption isotherms of NH_3 and CO_2, respectively (Fig. S5a and b†). Typically, the peaks observed under the low-temperature region (50–300 °C) determine the weak acid and base sites and, beyond, the active moderate/strongly acidic and basic sites. The pristine MgO has exhibited typical characteristics, *i.e.*, nearly 31 $\mu mol\ g^{-1}$ (acid sites) and 60–85 $\mu mol\ g^{-1}$ weak to moderate/strong (base sites)[14,16] (Table 2). Similarly, ZnO possessing amphoteric characteristics[36] had an equal acid strength (weak) to MgO, but with slight basicity (3–9 $\mu mol\ g^{-1}$ of weak to moderate/strong), therefore, it can play a significant role in the reaction by contributing to the number of weak basic sites (favorable for glucose interconversion) and suppressing the strong basicity of MgO in ZM11. The results of ZM11 evidenced the alterations enabled by the ZnO that it showed as high as has 121 $\mu mol\ g^{-1}$ of weak base sites with reduced strong basic sites (down to 48 $\mu mol\ g^{-1}$ from 60 $\mu mol\ g^{-1}$). However, its weak acidic sites were found to be doubled (60 $\mu mol\ g^{-1}$). These beneficial changes in the composite are attributed to the sturdy and synergic interaction between the metal oxides and the formed alloy (Zn–MgO), thereby exhibiting mixed characteristics of increased weak basicity but with a weak acidity. But the strategy was found to work only with the ZM11 formulation. Because the ZM21 exhibited similar acid–base characteristics as ZnO, *i.e.*, 31 μmol NH_3 per g and 4–12 μmol CO_2 per g, the result is reasonable as it has a higher ZnO concentration (Table 2). Therefore, it may not have a surface MgO and synthesize an alloy, which are said to be responsible for the basicity of a catalyst.[50] ZM12 containing a higher molar ratio of MgO exhibited corresponding characteristics, *i.e.*, 29 μmol NH_3 per g and 104–29 μmol CO_2 per g, ascribed to the large binding of MgO with ZnO, therefore, offered a relatively large surface area than ZM21 and weak acid sites predominantly. Similarly, it has not been involved in the formation of an alloy based on the XPS analysis. Of all the composites, ZM11 stood out with superior surface area and basicity parameters, attributed to mainly the alloy formation rather than the strong interaction between the metal oxides. Owing to the higher weak base sites[14] with reduced moderate/strong base sites by the impact of ZnO incorporation, ZM11 can be effective in the interconversion of glucose into fructose.

Effectiveness of the as-synthesized MgO/ZnO nanocomposite on glucose isomerization

Having confirmed the characteristics of ZM11 *via* comprehensive analytical techniques that it can expose maximum weak basicity, which is favorable for glucose interconversion,[14] its effectiveness was evaluated at 100 °C in water. The results testimony the nanocomposite's ability in the reaction by achieving 31.3% fructose yield and 82.8% selectivity through a 37.8% substrate conversion within 90 min. However, it enabled usual side product(s) formations, such as 2.5% mannose and 1.4% allulose, under basic conditions.[37] Its productivity is comparatively better than that of pristine and other composite catalysts under similar conditions (Fig. 4a and S7†). For example, the pristine ZnO exhibiting predominant weak acid sites has hardly promoted the conversion, achieving only 1.9% fructose and 67.97% selectivity through a 2.8% glucose conversion. This is likely caused by the inherently lower number of acidic sites that are not adequate for promoting the reaction in water. But it could control the unwanted reactions, as glucose normally encounters inevitable degradations under a chemical environment to form humin (an unstructured carbohydrate-derived product) prevalently.[6] Therefore, the loss of substrate was only 32% (relative) to yield, possibly HMF to a small extent,[9,38] excluding the untraceable humin, consistent with the carbon balance (Table S6†). The pristine MgO exhibiting a considerable number of weak and moderate/strong basic sites showed a contrary isomerization result, *i.e.*, producing 29.8% fructose but with a relatively lower selectivity of 56.4%

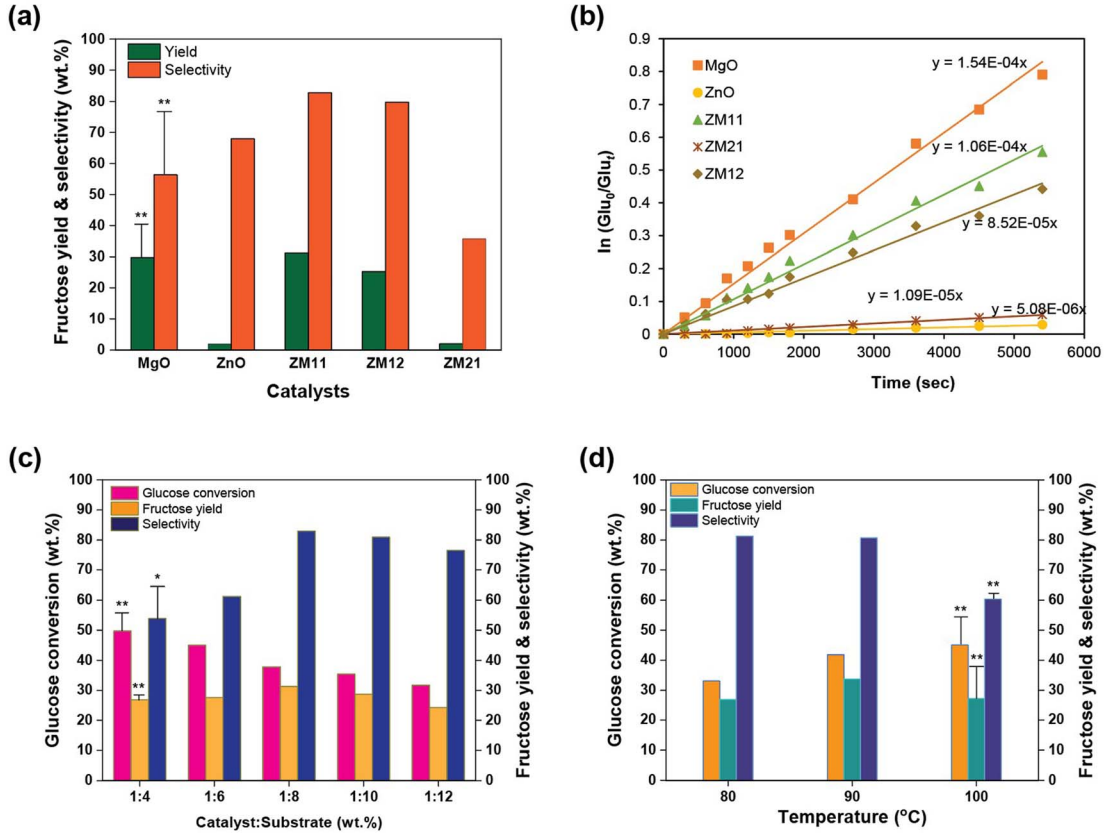

Fig. 4 Comparative results of glucose isomerization: (a) fructose formation over different catalysts at 100 °C and 1 : 8 wt catalyst loading on glucose after 90 min; (b) corresponding first-order kinetics of glucose isomerization in water over different catalysts up to 150 min; (c) effect of catalyst (ZM11) loading at 100 °C after 90 min; (d) effect of temperature at 12.5% catalyst loading after 120 min in an aqueous medium. The data are an average of two runs. The error bars represent the standard error. The asterisks * and ** denote the significant and non-significant nature of the mean data *via* two-way ANOVA analysis (at $\alpha = 0.05$).

(through 52.8% glucose conversion).[16] From this, the moderate/strong base can influence the unwanted degradations,[39] resulting in a 43% glucose consumption and 31% reduction in selectivity compared to ZnO. Whereas, the ZM21 composite exhibiting similar characteristics as ZnO (31 μmol g^{-1} weak acidic and 12 μmol g^{-1} weak basic sites) achieved an almost similar yield result of 2.1% fructose with 38.1% selectivity. The ZM12 containing a higher MgO concentration has shown an obvious efficiency similar to MgO (25.3% fructose yield and 79.7% selectivity) through a 31.7% glucose conversion. From the results of pristine MgO and ZM12, the aggressiveness of the strong basic sites in sugar degradation to unwanted products can be witnessed. Thus, the efficiency of ZM11, especially fructose selectivity, can be correlated to the weak basic sites generated by the synergism of metal oxides. The impact of basicity (both weak and moderate/strong) on glucose disappearance can be substantiated from the kinetic results determined by applying the assumptions (eqn (S7) and (S8)):† (i) the reactant and product molecules do not undergo a further equilibrium with other possible sugars (such as mannose using glucose and allulose using fructose as when forms)[16] and (ii) the conversion is first-order. The pristine MgO has accelerated the conversion with $r_{\text{Glu-MgO}} = 1.5 \times 10^{-4}$ s^{-1} (Fig. 4b), and contrarily, the ZnO exhibited a slower rate of glucose degradation with $r_{\text{Glu-ZnO}} = 5.1 \times 10^{-6}$ s^{-1}. Whereas, the ZM11 exhibited a bit faster rate, *i.e.*, $r_{\text{Glu-ZM11}} = 1.1 \times 10^{-4}$ s^{-1}, compared to other nanocomposites ($r_{\text{Glu-ZM21}} = 1.1 \times 10^{-5}$ s^{-1} and $r_{\text{Glu-ZM12}} = 8.5 \times 10^{-5}$ s^{-1}). Between ZM21 and ZM12, the latter's faster acceleration is attributed to the higher magnesium content. While correlating the findings of the analytical characterizations, the enabled glucose degradation with a better speed by the composites compared to ZnO is rational. However, the elemental composition had implications for glucose degradation. The superior kinetics of ZM11 can be interpreted as the increased catalytic sites offered by the MgO settled on a wider ZnO's surface and alloy formation (Zn–MgO) exhibiting a favorable weak base condition. This can be found consistent with the calculated turnover frequency (TOF; no. of moles of fructose formation to no. of active sites per unit time) in water at 90 min with a measure of 1.12×10^{-5} $mmol_{Fru}/mol_{Active\ site}/s$ for ZM11, 1.28×10^{-5} $mmol_{Fru}/mol_{Active\ site}/s$ for ZM12 and $\sim 1.0 \times 10^{-5}$ $mmol_{Fru}/mol_{Active\ site}/s$ for ZM21. Except for ZnO, all catalysts accompanied the production of mannose as a side product up to 3% formed *via* both glucose C2 epimerization and fructose C2 isomerization, regardless of the base characteristics. Under a base condition, its formation using glucose also

follows the LdB–AvE mechanism by synthesizing a *Z*-configuration enediol intermediate,[9,40] whose structure is such that it allows a rapid transfer of hydrogen between the two oxygens to form mannose and fructose parallelly.[37] However, the rate of glucose epimerization is slower than fructose isomerization to mannose due to the monosaccharide cyclization issues.[41] Assuming the weak acidic sites had nil effect on the side product interconversion, which is enabled *via* a contrary glucose C2–C1 carbon shift pathway.[42]

Subsequently, the optimization of the important processing parameters was carried out by employing a conventional technique, *i.e.*, varying one variable at a time. From the results of a varying catalyst load (ZM11) on glucose from 8–25% wt, the impact of the catalyst on glucose degradation is significant (Fig. 4c and S8a†). The glucose conversion and selectivity responses were found to fit a linear trend with $R^2 = 0.78$–0.94. The result also sanctions the proficiency of ZM11, in that, it could form significant fructose (24.3%) under a 12-times lower supply of catalyst on glucose. Maximum fructose yield was attained at 12.5% loading (likely attributed to a balanced ratio of the substrate and catalytic sites) and, beyond, attained a reduced fructose yield (from 31.2 to 26.9%), despite continuing glucose consumption (relatively 32%). This refers to the increased unwanted side reaction(s) (Table S6†) under high-severity conditions (*i.e.*, excess active sites, high temperature, and prolonged reaction), as discussed elsewhere.[6,16,38] Similarly, the responses were recorded under extended times by keeping other parameters constant. It can be seen that the shorter reaction times (<90 min) at 100 °C in water are not effective (<15% fructose yield) due to the impact of the catalyst's activation energy, but improved fructose's selectivity reaching 92%. The prolonged reaction of 90 min was found to be optimum, and a further extended reaction of up to 150 min resulted in reduced productivity (∼27% fructose and 56% selectivity) likely caused by the enhanced sugar degradation. The varying temperatures from 80 °C to 100 °C have influenced fructose production (Fig. 4d and S8b†); for example, at 80 °C, early 26.8% fructose and 81.3% selectivity were attained nafter 120 min. Typically, a prolonged reaction is operative under low-temperature conditions. In the raised temperature conditions, 90 °C was found to be the optimum (yielding 33.7% fructose and 80.7% selectivity after 120 min). A higher temperature (>90 °C) attained a significant reduction in productivity (20–25% yield and selectivity), caused by the reactant and product degradations through a relatively 8% higher glucose consumption (Table S7†).[9]

Effect of alcohol on glucose isomerization over MgO/ZnO nanocomposite

The parameter optimization suggested that the active sites (weak basic and acidic) offered by both MgO and ZnO are influential. From the literature employing basic or acidic catalysts, polar protic organic solvents, such as alcohols, can further improve productivity by stabilizing the transition state molecules (whose stabilization is important to control the unwanted product formations).[43] Based on the structure calculations, the OH moieties of the solvent or metal oxide can involve a charge compensation of the glucose anion resulting in an abstraction of a proton by the base catalyst and stabilization, thereby promoting the reaction synergistically.[44] Also, they can alter the shift in the glucose to fructose equilibrium towards fructose, thereby improving the fructose concentration. In a typical reaction, water is helpful,[9,15] ascribed to the relatively higher polarity, dielectric constant, and the extent of sugar dissolution and ionization properties, but it allows sugar degradation (to an extent). Therefore, many have supplemented alcohol in the reaction medium to improve product selectivity by controlling the side reactions. Considering alcohol's assistance in the reaction (enriched fructose formation), ethanol/methanol at different proportions from 4 : 1 to 1 : 1 vol water/alcohol was supplemented to the medium. The results obtained under optimum conditions evident the support of alcohol (Fig. S9†) by achieving 9–12% higher fructose selectivity than water medium (∼80.7%). However, the fructose formations varied depending on the concentration and property (probably dielectric constant, ε) of alcohol. For instance, the one-fourth ratio of alcohol to water achieved a nearly 26.9–32.3% fructose, while an equal ratio mixture attained a relatively lower yield (21–35%). This difference in the yield can be, at least, linked to the impact of sugar ionization and dissolution by an increased alcohol ratio, based on the results of the water medium (33.7%), though water allowed a higher sugar degradation (Table S8†) attributed to the mentioned properties. Comparatively, methanol (ε = 32.7) exhibited a better performance by achieving a relatively 20% higher fructose yield with 11% selectivity after 120 min than ethanol ($\varepsilon = 24.5$) (Fig. 5a), referring to the implication of ε-factor.[45] The results validated the assumption that alcohols can improve selectivity by regulating the undesired side reactions.[43] When the reaction was continued to 150 min, it attained a slightly improved fructose synthesis (35.5%) and selectivity (89.8%) with 0.8% of mannose and 1.13% of allulose formations (as byproducts) in W/MeOH (4 : 1 vol). The result is comparatively far better than that obtained on other catalyst formulations, including pristine metal oxides, *i.e.*, relatively 2 to 4-fold low, as shown in Fig. 5b. The prolonged reaction of up to 165 min exhibited a nominal difference in fructose formation and in fact, reduced the selectivity by 4–8% (relatively), pronouncing the impact of higher reaction severity.[38,46] Fig. 5b and S10† display the comparative result of glucose isomerization over MgO/ZnO pristine and composite catalysts in 4 : 1 W/MeOH. From the results, the system modification by employing methanol has little effect on fructose formation. But the improved selectivity (87.2–95.5%) with the catalysts having a higher ratio of ZnO (such as ZnO, ZM11 and ZM21) can be interpreted as the role of methanol in altering the ZnO's acidic properties based on the results of pristine ZnO in water and 4 : 1 W/MeOH vol mediums. The specificity of methanol in triggering the acidic sites of ZnO can be verified from the results of other catalysts (such as pristine MgO and ZM12), which offer a higher moderate/strong basicity, that attained similar productivity compared to the water medium (*i.e.*, 22.5–29.7% fructose yield and 48.8–79.7% selectivity under varying conditions). This suggests that ZnO's acidic sites also influence the

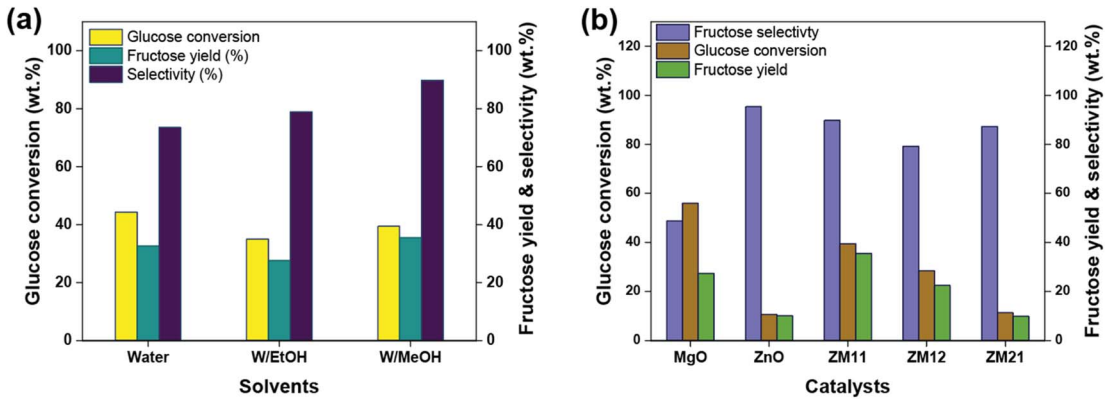

Fig. 5 Comparative results of glucose isomerization in aqueous-organic medium: (a) effect of alcohol on fructose formation over ZM11 at 90 °C up to 150 min and (b) productivity of different catalysts in W/MeOH (4 : 1) at 90 °C up to 150 min. The data are an average of two runs.

glucose transformation when the catalysis is performed in supplemented methanol medium (Table S9†). However, the kinetic trend was found to be as similar to an aqueous medium, *i.e.*, MgO and ZM11 had faster kinetics of $r_{\text{Glu-MgO}} = 1 \times 10^{-4}$ s^{-1} and $r_{\text{Glu-ZM11}} = 6 \times 10^{-5}$ s^{-1}, respectively, than others ($r_{\text{Glu-ZnO}} = 1 \times 10^{-5}$ s^{-1}, $r_{\text{Glu-ZM21}} = 1 \times 10^{-5}$ s^{-1} and $r_{\text{Glu-ZM12}} = 4 \times 10^{-5}$ s^{-1}) (Fig. S11†), suggesting that ZnO's influence is specifically on the reaction selectivity. The calculated turnover frequency in W/MeOH (4 : 1) at 150 min for the composites were 7.6×10^{-5} $mmol_{Fru}/mol_{Active\ site}/s$ for ZM11, 6.8×10^{-5} $mmol_{Fru}/mol_{Active\ site}/s$ for ZM12 and $\sim 1.0 \times 10^{-4}$ $mmol_{Fru}/mol_{Active\ site}/s$ for ZM21. Moreover, the results of ZM11 represent an achievement when compared to the literature, wherein complicated catalyst materials were employed (*e.g.*, NH_3-treated metal oxides, metal–organic frameworks (MOFs), modified zeolites, *etc.*) under elevated conditions (>100 °C) that afforded ~32–34% fructose and ~65–85% selectivity.[6,7,17]

Subsequently, the ZM11's recycling efficiency was evaluated. It resulted in similar productivity up to 5 times of recycling, with an average fructose yield of 35% and selectivity of 90% under optimum conditions (Fig. S12†). While verifying the structural characteristics of the recycled catalyst *via* XRD analysis, it retained the original configuration (Fig. S13†), suggesting a minimum deposition of impurities on the catalytic surface owing to the minimum development of unwanted side products, including humin, based on higher fructose selectivity (90%). The results also exemplify the coherence of the metal oxides *via* ionic interaction, resulting in controlled elemental leaching in a water/alcohol medium.

Confirmation of the reaction pathway and catalytic activity *via* NMR analysis

The presumption that the weak basic sites govern the glucose interconversion is based on the results of ZM11 (Fig. 4 and 5).

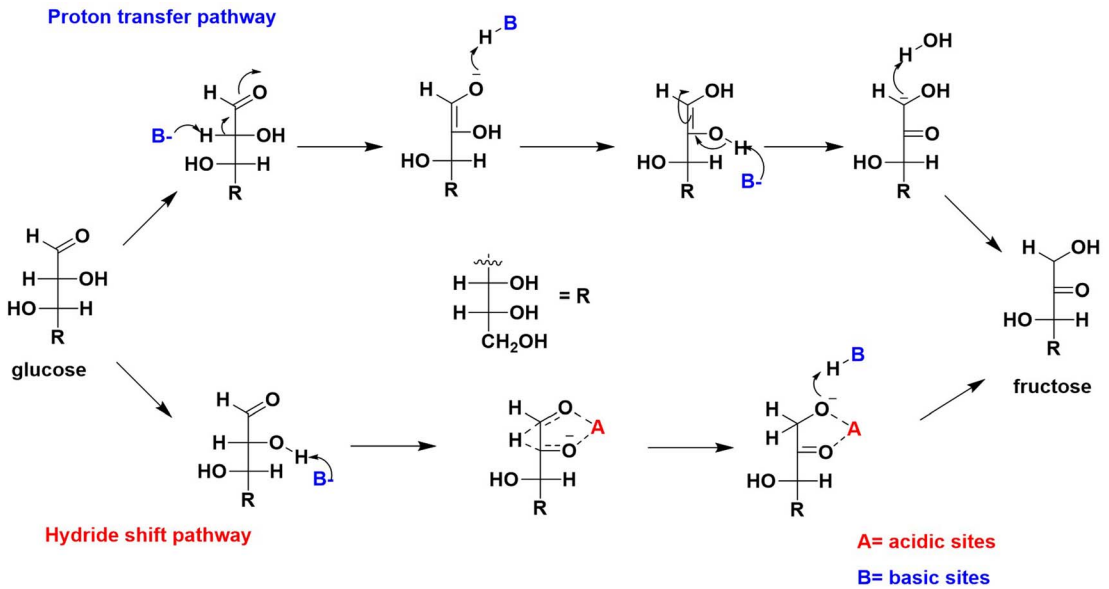

Scheme 1 Proposed mechanistic pathways of glucose into fructose influenced by the acidic and basic sites of a catalyst.

The incorporated amphoteric ZnO offering considerable weak acid sites has been involved actively in reducing strong basic sites of MgO *via* neutralization (Table 2), thereby controlling the unwanted sugar degradations. If so, the reaction should follow the principle of LdB–AvE by the formation of a 1,2-enediol intermediate *via* a proton transfer mechanism (Scheme 1).[9] By any chance, if the acidic sites of the composite were to influence the reaction, then it could have proceeded *via* a contrary 1,2-hydride shift mechanism to form fructose.[8] Under this circumstance, active participation of the basic or acidic sites can be delineated from the isotopic labelling experiments *via* NMR analysis.[38] For this experiment, two separate isomerization reactions were performed; in Exp-1, the labelled glucose (deuterated at C2) was used as a substrate in DI water, whereas in Exp-2, non-deuterated glucose was used but in D_2O medium under optimum conditions. The dislocation of deuterium between the C1–C2 positions in glucose/fructose can confirm the reaction pathway. When the transfer of deuterium from the medium to C2 of glucose due to the abstraction of a proton by MgO (assumption), the rearrangement can be interpreted as a base-catalyzed transformation through the formation of an enediol intermediate. The alternate mechanism can be confirmed through the migration of the deuterium from C2 to C1 of fructose when using the labelled glucose (at C2). Fig. 6 shows the comparative ^{13}C NMR spectra of the reference sugars (glucose and fructose) and the post-reaction mixture of Exp-1 and Exp-2. Firstly, the results confirm the formation of fructose over ZM11 in water based on the matching peaks. From the glucose's corresponding peak intensity, the substrate encounters a slight degradation to unwanted product(s) formation, consistent with the selectivity results (Fig. 4a–d). The product selectivity can be verified from the absence of any other irrelevant peaks in the spectra. In the spectra of post-reaction mixtures, the rigid and intense peaks observed at 98.04, 69.65, 69.17, 67.54, 63.86, and 63.33 ppm correspond to C2, C3, C4, C5, C1, and C6 carbon of α-D-fructopyranose. In water, fructose is available in three isomeric forms, such as β-D-fructopyranose, β-D-fructofuranose, and α-D-fructopyranose, which can be confirmed in the reference fructose spectrum. However, the post-reaction mixtures barely showed their presence, likely due to the higher residual glucose concentration than fructose. As a result, glucose can establish the two isomeric forms (such as β-D-glucopyranose and β-D-glucofuranose) in an aqueous medium based on the matching peaks with the reference glucose. When analyzing the ^1H NMR data (Fig. 7), the corresponding peaks of fructose from the reaction mixtures appear to merge. But, those can be seen matching with the reference fructose's peaks of β-D-fructopyranose and β-D-fructofuranose at $\delta = 3.62$ and 3.67 ppm, respectively.

Furthermore, while verifying the fructose formation pathways using the ^1H and ^{13}C spectra of Exp-1 and Exp-2 (as given in Fig. 6 and 7), a triplet observed at 73.64 and 70.94 ppm corresponding to the C2 carbon of the deuterated glucose confirmed the nil exchange of a proton between glucose and

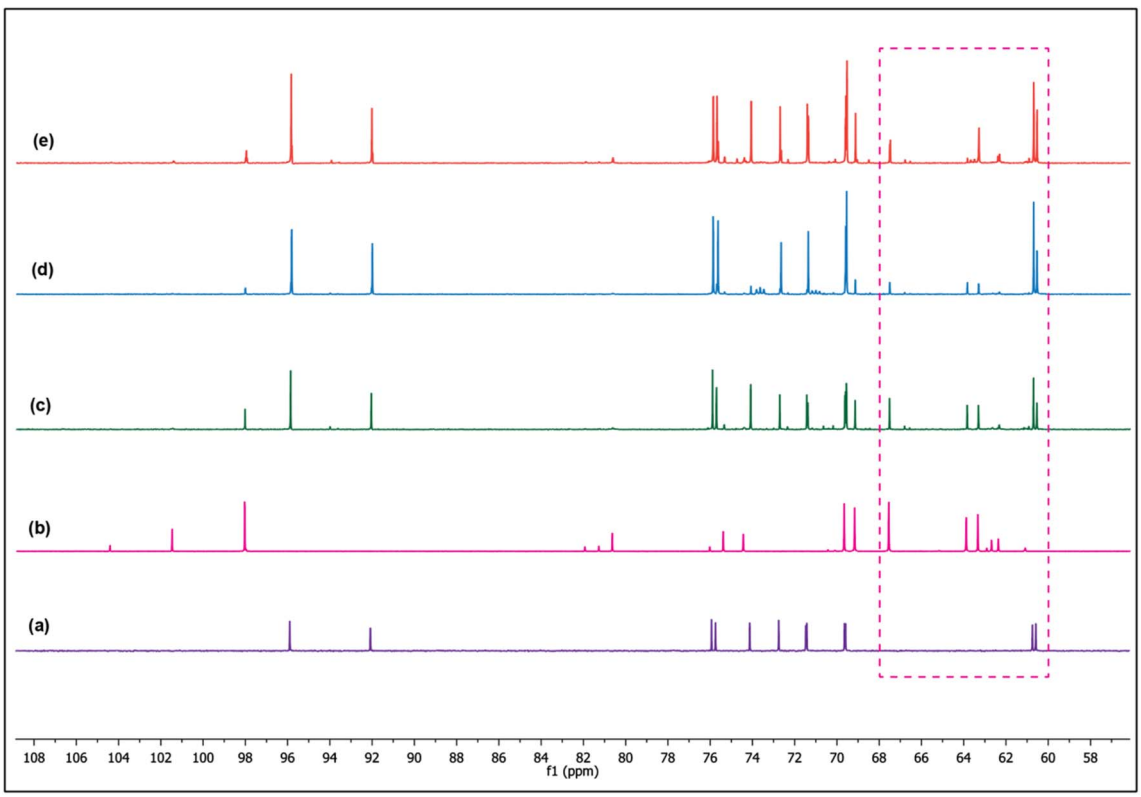

Fig. 6 ^{13}C spectra of (a) unlabelled glucose, (b) unlabelled fructose, (c) post-reaction mixture of reference glucose isomerization in water, (d) post-reaction mixture of labelled glucose isomerization in water, and (e) post-reaction mixture of unlabelled glucose isomerization in D_2O.

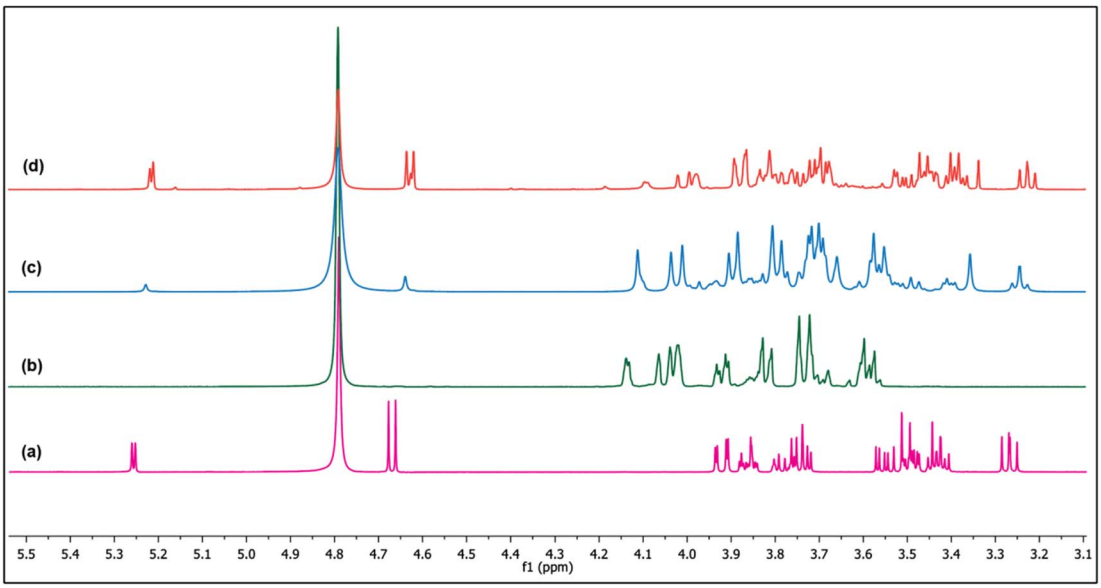

Fig. 7 ^{1}H NMR spectra of (a) unlabelled glucose, (b) unlabelled fructose, (c) post-reaction mixture of labelled glucose isomerization in water, and (d) post-reaction mixture of unlabelled glucose isomerization in D_2O.

water (medium). However, fructose exhibits a doublet at 63.86 and 63.30 ppm of C1 and C6 carbons, respectively. This can be explained in multiple ways by correlating the catalyst's activity; in one main aspect, the catalyst has acted as acid or base or otherwise in combination. If the reaction is progressed by the effect of weak acid sites, then the C1 carbon peak should represent a triplet due to the presence of the deuterium at C1 of fructose, but it remained a singlet (as can be noted in Fig. 6), suggesting the precedence of the reaction *via* a proton transfer pathway over the basic sites. In the event of coordinated activation of glucose conversion by both acidic and basic sites, the C1 of fructose should display both singlet and triplet forms, but it was not observed in the spectra of Exp-1 and Exp-2 (where glucose was isomerized in D_2O). Moreover, the ^{1}H NMR spectrum (Fig. 7) displays the extinction of peaks at 3.56 and 3.54 ppm of C1 (fructose), suggesting a probable occurrence of the proton transfer mechanism. Similarly, the ^{13}C NMR spectrum of Exp-2 displays (Fig. 6) an intense triplet instead of a singlet due to the presence of the deuterium, which can split the C1 carbon peak caused by the nuclear Overhauser effect (NOE).[38,47] Thus, the results authenticate the major reaction pathway *via* a proton transfer mechanism ascribed to the catalyst's basic effect. This can be further confirmed by quantitative NMR analysis (*q*NMR). In Fig. 8, Exp-1 shows four peaks at 63.86, 63.28, 62.65, and 62.27 ppm corresponding to C1 and C6 of fructose of two isomeric forms (β-D-fructopyranose and β-D-fructofuranose). Upon the integration of the peaks, no significant fall in C1's peak intensity (hardly a 1% difference) was observed when compared to C6, suggesting that the carbons have almost the same chemical environment. This slight reduction in C1's intensity can be correlated to deuterated fructose formation by the acidic sites' effect promoting the 1,2-hydride shift mechanism. Thus, the analysis confirmed glucose's maximum proton transfer mechanism into fructose.

Based on the NMR analysis, a plausible reaction mechanism can be proposed. From the optimization results, ZM11 exposing maximum weak basic sites is promising and can enable the conversion *via* proton transfer (or LdB–AvE mechanism). Moreover, ZM11 has surface-attached MgO nanoparticles and Zn–MgO alloy; characteristically, both can provide the basicity for the reaction. As it is understood, ZnO can also provide acidic sites, the maximum of which can be engaged in the neutralization of the strong basic sites of MgO. As per the TPD results, a few sites are in the free form. Therefore, MgO offering weak basic sites can promote the reaction. In that case, MgO can form a strong complex with glucose at C2 (Scheme 2) through an interaction, resulting in the development of a 1,2-dienediol intermediate due to deprotonation at C2.[16] This is likely possible in a basic medium established by exposed Mg–OH species, whose formation can be by an interaction between the catalyst's surface deposited MgO and surrounding water molecules. The resultant is an unstable compound, which can be stabilized by the glucose–MgO complex. However, the complex molecule can also be influenced by the moderate/strong basic sites of MgO to undergo unwanted glucose degradations. This unwanted activity can be controlled by the ZnO present in the composite *via* the suppression of the strong basic sites, thereby allowing the composite to expose a higher number of weak basic sites. In this way, the composite could enable a selective glucose conversion. Eventually, the complex molecule involved in a proton transfer from the Mg–OH to the oxygen of the C1 carbon *via* a four-membered transition state ultimately forms fructose.

Green matrices of the glucose interconversion process

From an upscaling perspective, the green metric parameters (such as environmental factor (*E*-factor), process mass intensity

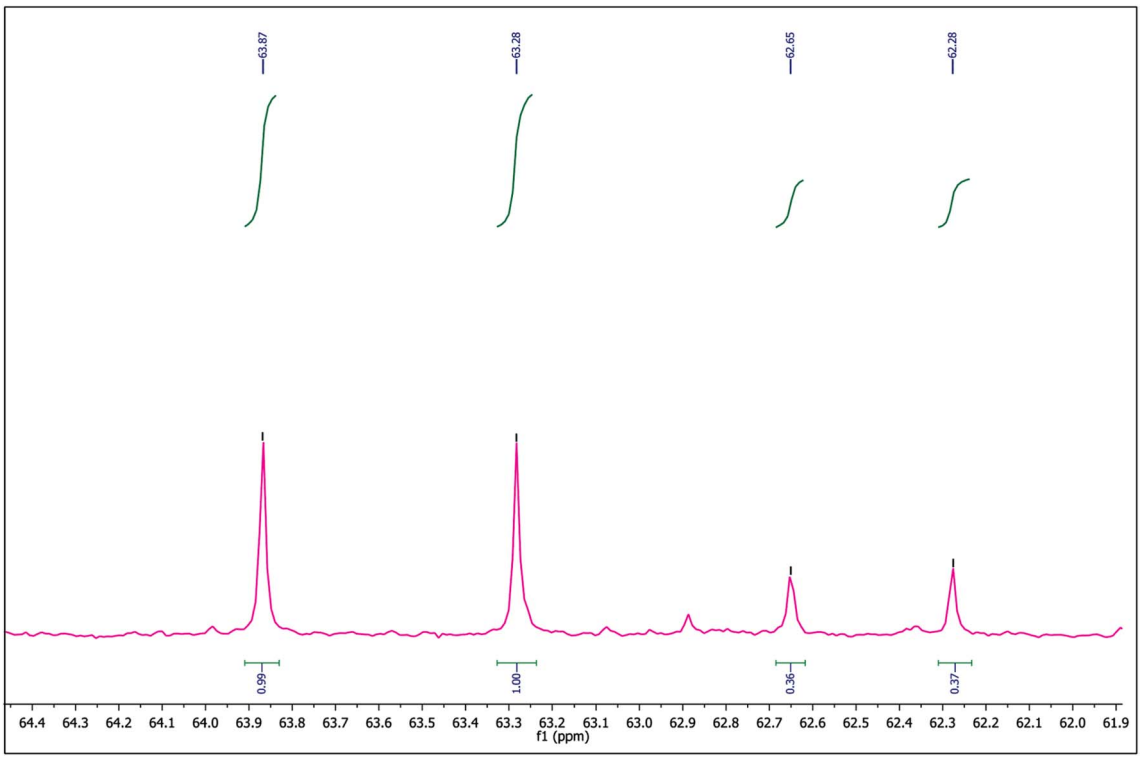

Fig. 8 Quantitative ^{13}C NMR report of labelled glucose isomerization in water.

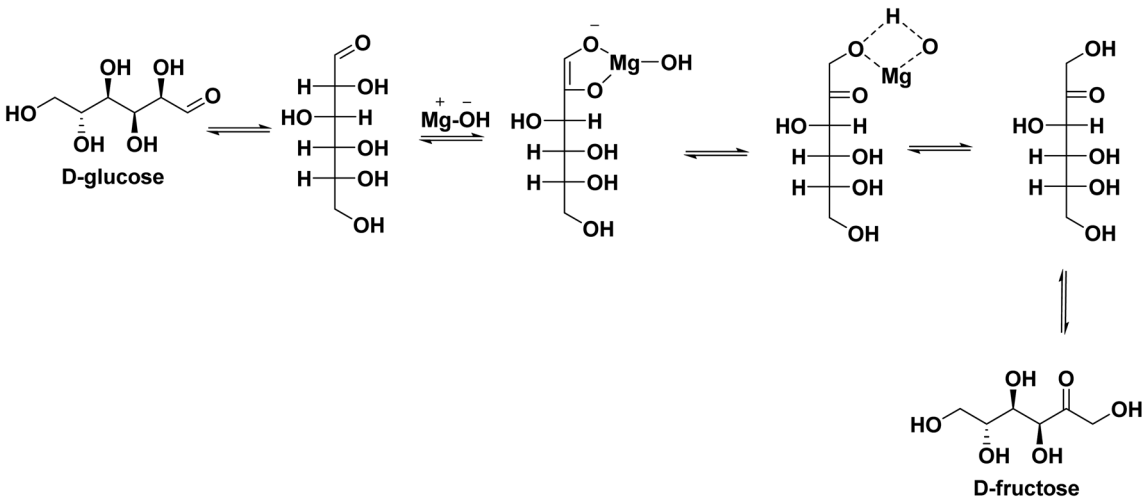

Scheme 2 The proposed mechanism of glucose isomerization to fructose over ZM11 (for the sake of clarity, MgO's interaction is only denoted here).

(PMI), atom economy (AE), and carbon efficiency (CE%)) of the glucose interconversion to fructose process were calculated.[48,49] These parameters normally determine a chemical process's feasibility and sustainability. For example, the *E*-factor signifying the process's environmental impact by accounting for the waste disposal should range between 1 and 5 for a chemical process. In this case, the value was found to be within the range (E = 1.67) (Table S10†). The PMI signifying a process's sustainability (*i.e.*, mass of reactant to the mass of product formation) was estimated to be 2.67, which is on the slightly higher side when compared to the value of an ideal process (PMI = 1.0). This deviation is likely caused by the reverse formation of glucose by using fructose (product). Moreover, the process's AE was found to be 100%, establishing a good conversion efficiency of reactant into products. The carbon efficiency of the reaction was obtained as 37.44.

Conclusions

The present study demonstrated the strategy of fine-tuning the base characteristics of the widely available MgO using the amphoteric ZnO and the efficiency of the MgO/ZnO nanocomposite in a selective glucose conversion to fructose. The characteristic MgO possesses both weak and moderate/strong basic sites, but only the Lewis basicity is favorable for selective glucose conversion. Upon blending of MgO with ZnO at an equal ratio, ZnO accommodated maximum MgO on its surface *via* pore blockage (*i.e.*, Mg into ZnO's framework), with an even dispersion trend, and reduced the unfavorable medium/strong basicity significantly. Thus, the nanocomposite offering maximum weak basic sites (mainly attributed to a Zn–MgO alloy formation) exhibited promising performance by achieving as high as 36% fructose yield and 90% selectivity under modest conditions in a water/methanol medium. The result is comparatively better than that from the literature employing a complex catalyst under elevated conditions. Moreover, the MgO/ZnO (1 : 1 wt ratio) exhibited good durability during recycling. From the NMR analysis, it is found that the interconversion reaction is dominated by the proton transfer pathway attributed to the weak basic sites offered by the surface-deposited MgO and Zn–MgO alloy. The insights into the fine-tuning of crucial characteristics of a solid catalyst will help design other inexpensive heterogeneous catalysts to produce fructose at a relatively cheaper cost towards a feasible bioenergy development.

Author contributions

Sangeeta Mahala, Senthil M. Arumugam and Sasikumar Elumalai: conceptualization, methodology, investigation, original draft preparation. Sangeeta Mahala, Senthil M. Arumugam, Sandeep Kumar, and Bhawana Devi: data analysis, writing – reviewing and editing. Sasikumar Elumalai: visualization, supervision, writing – reviewing, and editing.

Conflicts of interest

The authors do not have conflicts of interest to declare.

Acknowledgements

Sangeeta Mahala thanks the Department of Biotechnology (DBT), New Delhi, for the financial support through the Senior Research Fellowship (Flagship Project Grant No. BT/CIAB-Flagship/2018). The authors thank the Department of Biotechnology (DBT), New Delhi, for their consistent financial support and laboratory cum instrument facilities.

References

1 R.-J. van Putten, J. C. van der Waal, E. de Jong, C. B. Rasrendra, H. J. Heeres and J. G. de Vries, Hydroxymethylfurfural, A Versatile Platform Chemical Made from Renewable Resources, *Chem. Rev.*, 2013, **113**(3), 1499–1597.

2 A. Mittal, H. M. Pilath and D. K. Johnson, Direct Conversion of Biomass Carbohydrates to Platform Chemicals: 5-Hydroxymethylfurfural (HMF) and Furfural, *Energy Fuels*, 2020, **34**(3), 3284–3293.

3 C. Zhou, J. Zhao, A. E. A. Yagoub, H. Ma, X. Yu, J. Hu, X. Bao and S. Liu, Conversion of glucose into 5-hydroxymethylfurfural in different solvents and catalysts: Reaction kinetics and mechanism, *Egypt. J. Pet.*, 2017, **26**(2), 477–487.

4 L. M. Hanover and J. S. White, Manufacturing, composition, and applications of fructose, *Am. J. Clin. Nutr.*, 1993, **58**(5), 724s–732s.

5 S. H. Bhosale, M. B. Rao and V. V. Deshpande, Molecular and industrial aspects of glucose isomerase, *Microbiol. Rev.*, 1996, **60**(2), 280–300.

6 I. Delidovich and R. Palkovits, Catalytic Isomerization of Biomass-Derived Aldoses: A Review, *ChemSusChem*, 2016, **9**(6), 547–561.

7 H. Li, S. Yang, S. Saravanamurugan and A. Riisager, Glucose Isomerization by Enzymes and Chemo-catalysts: Status and Current Advances, *ACS Catal.*, 2017, **7**(4), 3010–3029.

8 Y. Román-Leshkov, M. Moliner, J. A. Labinger and M. E. Davis, Mechanism of Glucose Isomerization Using a Solid Lewis Acid Catalyst in Water, *Angew. Chem., Int. Ed.*, 2010, **49**(47), 8954–8957.

9 J. M. Carraher, C. N. Fleitman and J.-P. Tessonnier, Kinetic and Mechanistic Study of Glucose Isomerization Using Homogeneous Organic Brønsted Base Catalysts in Water, *ACS Catal.*, 2015, **5**(6), 3162–3173.

10 M. Ventura, J. Mazarío and M. E. Domine, Isomerization of Glucose-to-Fructose in Water over a Continuous Flow Reactor using Ca–Al Mixed Oxide as Heterogeneous Catalyst, *ChemCatChem*, 2022, **14**(3), e202101229.

11 Y. Li, X. Meng, R. Luo, H. Zhou, S. Lu, S. Yu, P. Bai, X. Guo and J. Lyu, Aluminum/Tin-doped UiO-66 as Lewis acid catalysts for enhanced glucose isomerization to fructose, *Appl. Catal., A*, 2022, **632**, 118501.

12 P. Drabo, M. Fischer, V. Toussaint, F. Flecken, R. Palkovits and I. Delidovich, What are the catalytically active species for aqueous-phase isomerization of D-glucose into D-fructose in the presence of alkaline earth metal (hydr) oxides?, *J. Catal.*, 2021, **402**, 315–324.

13 S. Kumar, D. Nepak, S. K. Kansal and S. Elumalai, Expeditious isomerization of glucose to fructose in aqueous media over sodium titanate nanotubes, *RSC Adv.*, 2018, **8**(53), 30106–30114.

14 A. A. Marianou, C. M. Michailof, D. K. Ipsakis, S. A. Karakoulia, K. G. Kalogiannis, H. Yiannoulakis, K. S. Triantafyllidis and A. A. Lappas, Isomerization of Glucose into Fructose over Natural and Synthetic MgO Catalysts, *ACS Sustainable Chem. Eng.*, 2018, **6**(12), 16459–16470.

15 A. A. Marianou, C. M. Michailof, A. Pineda, E. F. Iliopoulou, K. S. Triantafyllidis and A. A. Lappas, Glucose to Fructose Isomerization in Aqueous Media over Homogeneous and

Heterogeneous Catalysts, *ChemCatChem*, 2016, **8**(6), 1100–1110.

16 S. M. Arumugam, D. Singh, S. Mahala, B. Devi, S. Kumar, S. Jakhu and S. Elumalai, MgO/CaO Nanocomposite Facilitates Economical Production of d-Fructose and d-Allulose Using Glucose and Its Response Prediction Using a DNN Model, *Ind. Eng. Chem. Res.*, 2022, **61**(6), 2524–2537.

17 R. Otomo, M. Fujimoto, M. Nagao and Y. Kamiya, Ammonia-treated metal oxides as base catalysts for selective isomerization of glucose in water, *Mol. Catal.*, 2019, **475**, 110479.

18 A. I. M. Rabee, S. D. Le and S. Nishimura, MgO-ZrO2 Mixed Oxides as Effective and Reusable Base Catalysts for Glucose Isomerization into Fructose in Aqueous Media, *Chem.–Asian J.*, 2020, **15**(2), 294–300.

19 E. A. Pidko, V. Degirmenci and E. J. M. Hensen, On the Mechanism of Lewis Acid Catalyzed Glucose Transformations in Ionic Liquids, *ChemCatChem*, 2012, **4**(9), 1263–1271.

20 B. Cai, J. Feng, D. Guo, S. Wang, T. Ma, T. L. Eberhardt and H. Pan, Highly efficient isomerization of glucose to fructose over a novel aluminum doped graphitic carbon nitride bifunctional catalyst, *J. Cleaner Prod.*, 2022, **346**, 131144.

21 S. S. Chen, D. C. W. Tsang and J.-P. Tessonnier, Comparative investigation of homogeneous and heterogeneous Brønsted base catalysts for the isomerization of glucose to fructose in aqueous media, *Appl. Catal., B*, 2020, **261**, 118126.

22 A. Wang, W. Quan, H. Zhang, H. Li and S. Yang, Heterogeneous ZnO-containing catalysts for efficient biodiesel production, *RSC Adv.*, 2021, **11**(33), 20465–20478.

23 S. Raha and M. Ahmaruzzaman, ZnO nanostructured materials and their potential applications: progress, challenges and perspectives, *Nanoscale Adv.*, 2022, **4**(8), 1868–1925.

24 R. E. Adam, H. Alnoor, G. Pozina, X. Liu, M. Willander and O. Nur, Synthesis of Mg-doped ZnO NPs via a chemical low-temperature method and investigation of the efficient photocatalytic activity for the degradation of dyes under solar light, *Solid State Sci.*, 2020, **99**, 106053.

25 M. J. Limo, A. Sola-Rabada, E. Boix, V. Thota, Z. C. Westcott, V. Puddu and C. C. Perry, Interactions between Metal Oxides and Biomolecules: from Fundamental Understanding to Applications, *Chem. Rev.*, 2018, **118**(22), 11118–11193.

26 L. S. Rao, T. V. Rao, S. Naheed and P. V. Rao, Structural and optical properties of zinc magnesium oxide nanoparticles synthesized by chemical co-precipitation, *Mater. Chem. Phys.*, 2018, **203**, 133–140.

27 Y. Sun, Y. Jiang, H. Peng, J. Wei, S. Zhang and S. Chen, Efficient quantum dot light-emitting diodes with a Zn0.85Mg0.15O interfacial modification layer, *Nanoscale*, 2017, **9**(26), 8962–8969.

28 S. Vallejos, N. Pizúrová, I. Gràcia, C. Sotelo-Vazquez, J. Čechal, C. Blackman, I. Parkin and C. Cané, ZnO Rods with Exposed {100} Facets Grown via a Self-Catalyzed Vapor–Solid Mechanism and Their Photocatalytic and Gas Sensing Properties, *ACS Appl. Mater. Interfaces*, 2016, **8**(48), 33335–33342.

29 Z. Wang, H. Li, F. Tang, J. Ma and X. Zhou, A Facile Approach for the Preparation of Nano-size Zinc Oxide in Water/Glycerol with Extremely Concentrated Zinc Sources, *Nanoscale Res. Lett.*, 2018, **13**(1), 202.

30 M. Claros, M. Setka, Y. P. Jimenez and S. Vallejos, AACVD Synthesis and Characterization of Iron and Copper Oxides Modified ZnO Structured Films, *Nanomaterials*, 2020, **10**(3), 471.

31 L. F. Leopold, C. Coman, D. Clapa, I. Oprea, A. Toma, S. D. Iancu, L. Barbu-Tudoran, M. Suciu, A. Ciorîtă, A. I. Cadis, L. E. Muresan, I. M. Perhaita, L. Copolovici, D. M. Copolovici, F. Copaciu, N. Leopold, D. C. Vodnar and V. Coman, The effect of 100–200 nm ZnO and TiO2 nanoparticles on the in vitro-grown soybean plants, *Colloids Surf., B*, 2022, **216**, 112536.

32 Y. V. Kaneti, Q. M. D. Zakaria, Z. Zhang, C. Chen, J. Yue, M. Liu, X. Jiang and A. Yu, Solvothermal synthesis of ZnO-decorated α-Fe2O3 nanorods with highly enhanced gas-sensing performance toward n-butanol, *J. Mater. Chem. A*, 2014, **2**(33), 13283–13292.

33 C. Zhou, Y. Wang, L. Du, H. Yao, J. Wang and G. Luo, Precipitation Preparation of High Surface Area and Porous Nanosized ZnO by Continuous Gas-Based Impinging Streams in Unconfined Space, *Ind. Eng. Chem. Res.*, 2016, **55**(46), 11943–11949.

34 H. Kitajima, H. Yoshimasa, M. Shiho, Z. Heng, W. Masaru, M. A. Taku and L. S. Richard Jr, Isomerization of glucose at hydrothermal condition with TiO_2, ZrO_2, CaO-doped ZrO_2 or TiO_2-doped ZrO_2, *Catal. Today*, 2016, **274**, 67–72.

35 Y. Liu, G. Ding, H. Wang, X. Li, J. Zhang, Y. Zhu, Y. Yang and Y. Li, Highly selective glucose isomerization by HY zeolite in gamma-butyrolactone/H2O system over fixed bed reactor, *Catal. Commun.*, 2021, **156**, 106324.

36 J. Wang, R. Chen, L. Xiang and S. Komarneni, Synthesis, properties and applications of ZnO nanomaterials with oxygen vacancies: A review, *Ceram. Int.*, 2018, **44**(7), 7357–7377.

37 S. Kumar, S. M. Arumugam, S. Sharma, S. Mahala, B. Devi and S. Elumalai, Insights into the kinetics and mechanism of spermine (base)-catalyzed D-fructose interconversion to low-calorie D-allulose, *Mol. Catal.*, 2022, **533**, 112757.

38 C. G. Yoo, N. Li, M. Swannell and X. Pan, Isomerization of glucose to fructose catalyzed by lithium bromide in water, *Green Chem.*, 2017, **19**(18), 4402–4411.

39 M. Fischer, P. Drabo and I. Delidovich, Study of base-catalyzed isomerization of d-glucose with a focus on reaction kinetics, *React. Kinet., Mech. Catal.*, 2022, **135**(5), 2357–2377.

40 G. De Wit, A. Kieboom and H. Van Bekkum, Enolisation and isomerisation of monosaccharides in aqueous, alkaline solution, *Carbohydr. Res.*, 1979, **74**(1), 157–175.

41 H. Isbell, H. Frush, C. Wade and C. Hunter, Transformations of sugars in alkaline solutions, *Carbohydr. Res.*, 1969, **9**(2), 163–175.

42 N. Rodriguez Quiroz, A. M. Norton, H. Nguyen, E. Vasileiadou and D. G. Vlachos, Homogeneous Metal Salt

Solutions for Biomass Upgrading and Other Select Organic Reactions, *ACS Catal.*, 2019, **9**(11), 9923–9952.

43 M. Yabushita, N. Shibayama, K. Nakajima and A. Fukuoka, Selective Glucose-to-Fructose Isomerization in Ethanol Catalyzed by Hydrotalcites, *ACS Catal.*, 2019, **9**(3), 2101–2109.

44 G. Li, E. A. Pidko and E. J. M. Hensen, Synergy between Lewis acid sites and hydroxyl groups for the isomerization of glucose to fructose over Sn-containing zeolites: a theoretical perspective, *Catal. Sci. Technol.*, 2014, **4**(8), 2241–2250.

45 D.-M. Gao, T. Kobayashi and S. Adachi, Promotion or suppression of glucose isomerization in subcritical aqueous straight- and branched-chain alcohols, *Biosci., Biotechnol., Biochem.*, 2015, **79**(3), 470–474.

46 C. Liu, J. M. Carraher, J. L. Swedberg, C. R. Herndon, C. N. Fleitman and J.-P. Tessonnier, Selective Base-Catalyzed Isomerization of Glucose to Fructose, *ACS Catal.*, 2014, **4**(12), 4295–4298.

47 H. Nguyen, V. Nikolakis and D. G. Vlachos, Mechanistic Insights into Lewis Acid Metal Salt-Catalyzed Glucose Chemistry in Aqueous Solution, *ACS Catal.*, 2016, **6**(3), 1497–1504.

48 R. Sharma, A. Selim, B. Devi, S. M. Arumugam, S. Sartaliya, S. Elumalai and G. Jayamurugan, *Realizing direct conversion of glucose to furfurals with tunable selectivity utilizing a carbon dot catalyst with dual acids controlled by a biphasic medium*, Biomass Conversion and Biorefinery, 2022.

49 J. H. Clark, T. J. Farmer, D. J. Macquarrie and J. Sherwood, Using metrics and sustainability considerations to evaluate the use of bio-based and non-renewable Brønsted acidic ionic liquids to catalyse Fischer esterification reactions, *Sustainable Chem. Processes*, 2013, **1**(1), 23.

50 S. Mondal, A. A. Arifa and P. Biswas, Production of 1,2-propanediol from renewable glycerol over highly stable and efficient Cu–Zn (4 : 1)/MgO catalyst, *Catal. Lett.*, 2017, **147**, 2783–2798.